Study on the Mechanism Model of the Influence of IGBT Device Health Status on Electromagnetic Voiceprint Signals

Shuzhi Wen, *Student Member, IEEE*, Bingkun Wei, *Member, IEEE*, Lisha Peng, *Senior Member, IEEE*, Pu Huang, *Member, IEEE*, Shisong Li, *Senior Member, IEEE*, and Songling Huang, *Senior Member, IEEE*

***Abstract*—State monitoring technology is essential for the fault prognostics and health management of power electronic devices. Electromagnetic voiceprint (EMVP) signals, produced during the switching transients of these devices, carry substantial information about their health status. In recent years, EMVP signals have gained attention as a promising state monitoring indicator for power electronic devices. However, the mechanism by which the health status of a device affects its EMVP signals remains unclear, limiting their use in health monitoring. This article investigates the impact of insulated gate bipolar transistor (IGBT) health status on EMVP signals and develops a mechanistic model to illustrate the influence of bond wire lift-off and solder aging on EMVP signals. Simulation models were developed to analyze the impact of both scenarios on EMVP signals. Typical features are proposed to characterize the relationship between IGBT health status and EMVP signal. Experimental validation supports the theoretical framework and simulation results. The research provides a theoretical foundation for the development of reliability evaluation methods based on EMVP.**

***Index Terms*—Bonding wire lift-off, condition monitoring, electromagnetic voiceprint (EMVP), influencing factor mechanism model, insulated gate bipolar transistor (IGBT), solder aging.**

I. Introduction

POWER electronics technology leverages power electronic devices for the conversion of electrical energy and plays a vital role in new energy generation and high-voltage direct current transmission systems [1], [2], [3], [4], [5]. Traditional methods to enhance the reliability of power electronic devices, such as redundancy and derating operation, are no longer sufficient to meet the rapidly growing safety requirements of these systems [6], [7]. The prognostics and health management (PHM) techniques for power electronic devices can take preventive measures before device failure, thereby reducing losses and incidents, and effectively improving the operational reliability of both the devices and the systems [8], [9]. In this context, monitoring the health status of the devices is essential for effective fault prediction and health management.

Power electronic devices are commonly monitored using techniques such as thermistor-based electrical parameter monitoring [10], [11], [12], optical monitoring [13], [14], and magnetic field monitoring [15], [16]. These conventional methods, however, are limited by low resolution, invasiveness, and the complexity of their monitoring circuits. Electromagnetic voiceprint (EMVP) signals are mechanical stress waves generated by power electronic devices during switching operations. The signals provide valuable insights into the health status of power electronic devices. The appeal of EMVP-based condition monitoring methods lies in their noninvasiveness and heightened sensitivity, garnering widespread research attention in recent years.

Karkkainen and colleagues were the first to observe that IGBT modules emit EMVP signals during switching operations [17]. By analyzing the time differences in EMVP signals captured by multiple sensors, they further identified the source of the sound as being near the IGBT chip [18]. Subsequently, an increasing number of scholars have begun to investigate the correlation between EMVP phenomena and the operational states of devices. Kozak and Gordon [19] employed broadband acoustic emission (AE) sensors to capture and spectrally analyze the sound signal waveforms of IGBT transistors. Bejger et al. [20] examined EMVP signal waveforms and identified their correlation with parasitic parameters. They further explored the temperature's effect, noting a potential EMVP decrease with rising temperatures [21]. EMVP signal generation is tied to switching electromagnetic transients, making it intimately connected to electrical parameters. Li et al. [22] discovered a strong correlation between low-frequency EMVP components and IGBT turn-OFF current, with high-frequency components showing no correlation. Bai et al. [23] confirmed EMVP's viability for condition monitoring by assessing factors like sensor position and electrical parameters in MOSFET. Geng et al. [24] measured the IGBT EMVP with a differential probe revealed the effects

Received 11 November 2024; revised 21 December 2024 and 9 January 2025; accepted 2 February 2025. Date of publication 5 February 2025; date of current version 20 March 2025. This work was supported in part by the National Key Research and Development Program of China under Grant 2022YFF0605600 and in part by the Natural Science Foundation of China under Grant 52477008 and Grant U23B20113. Recommended for publication by Associate Editor D. Peftitsis. *(Corresponding author: Songling Huang.)*

The authors are with the State Key Laboratory of Power System Department of Electrical Engineering, Tsinghua University, Beijing 10084, China (e-mail: wensz21@mails.tsinghua.edu.cn; weibingkun@tsinghua.edu.cn; penglisha@tsinghua.edu.cn; huang_pu@buaa.edu.cn; shisongli@tsinghua.edu.cn; huangsling@tsinghua.edu.cn).

Color versions of one or more figures in this article are available at https://doi.org/10.1109/TPEL.2025.3538987.

Digital Object Identifier 10.1109/TPEL.2025.3538987

of bus voltage and turn-OFF resistance on signal intensity. While experimental studies have provided valuable insights into EMVP characteristics in power electronic devices, a comprehensive theoretical framework is still lacking. And the application of EMVP for comprehensive health status assessment has not yet been fully exploited.

EMVP contains abundant information about the condition of power electronic devices, including their health status. Muller et al. [25] investigated the frequency spectrum differences of EMVP in IGBT modules before and after aging. Davari [26] proposed an assessment method based on characteristic frequency peaks, derived from power cycling tests. Bejger et al. [27] identified differences in the power spectral density of EMVP between normal and faulty states. Similarly, Kozak and Gordon [28] compared the frequency domain characteristics of EMVP under various damage conditions, finding additional frequencies emerging near the damage points. However, these studies are primarily based on empirical observations and do not explore the underlying monitoring mechanisms. This limits their reliability in practical applications. In terms of theoretical research, only Geng et al. [29] have studied the generation mechanism of EMVP. They suggested that EMVP is mainly produced by the Lorentz force and thermal expansion effects. However, their study focused only on EMVP signals generated within the IGBT chip and did not address the mechanisms of EMVP signal generation in the power device packaging. In summary, there is a significant gap in research regarding the mechanisms by which the health status of power devices influences EMVP.

To address these issues, this article investigates the mechanism model of EMVP signal generation in IGBT devices, focusing on their packaging structure. Based on this, the effects of bond wire lift-off and solder layer defects on EMVP signals are studied. Corresponding mechanistic and finite element simulation models are proposed to explain the changes in EMVP signals before and after the degradation of packaging reliability. Finally, the validity of the theoretical and simulation models is verified through experiments.

The rest of this article is organized as follows. Section II introduces the mechanism model. Section III develops finite element simulation models to investigate the variations in EMVP signals. Section IV presents experiments to validate the theoretical and simulation models. Section V discusses the mechanism model and EMVP health monitoring methods. Finally, Section VI concludes this article.

II. Mechanism Model of EMVP Under the Influence of Packaging Structure

A. Generation Mechanism of EMVP

Existing studies have shown that the EMVP in power electronic devices is generated by the combined effects of the ampere force and thermal expansion effects [29]. The stress and strain induced by the ampere force are calculated using elasticity theory, while the thermal stress and strain resulting from temperature variations are calculated using thermoelastic theory. From the perspective of strain, the total strain tensor of an object is a linear function of both the stress tensor components ε_{ij}^{e} and the temperature strain tensor components ε_{ij}^{T} as follows:

$$\varepsilon_{ij} = \varepsilon_{ij}^{e} + \varepsilon_{ij}^{T}, \qquad i, j = 1, 2, 3. \tag{1}$$

According to the linear elastic and linear thermoelastic constitutive relationships. The total strain tensor ε_{ij} can be expressed as follows:

$$\varepsilon_{ij} = \frac{1}{2\mu}\left(\tau_{ij} - \frac{\lambda}{3\lambda + 2\mu}\tau_{kk}\delta_{ij}\right) + \alpha\left(T - T_0\right)\delta_{ij}. \tag{2}$$

Here, λ and μ are Lamé parameters, τ_{ij} is the stress tensor, α is the linear coefficient of thermal expansion, T is the temperature, and δ_{ij} is the Kronecker delta symbol. The elastic equilibrium equation can be written as follows:

$$\tau_{ij,j} + F_i = \rho\ddot{u}_i. \tag{3}$$

Here, F_i represents the body force, ρ is the material density, and $\ddot{u}_i$ denotes the acceleration. Under the assumptions of linear approximation and small strains, the strain-displacement equation can be expressed as follows:

$$\varepsilon_{ij} = \frac{1}{2}\left(u_{i,j} + u_{j,i}\right). \tag{4}$$

Here, u is the displacement field of the medium. Using the relationship given in (2), the stress can be expressed in terms of strain. Applying (4), the wave equation in an isotropic elastic medium can be obtained as follows:

$$(\lambda + \mu)\, u_{j,ij} + \mu u_{i,jj} - (3\lambda + 2\mu)\alpha T_{,i} + \rho f_i = \rho\ddot{u}_i. \tag{5}$$

Here, f_i is the body force per unit volume. Compared to the conventional wave equation [30], the third term on the left-hand side (LHS) of (5) incorporates the effect of thermal expansion stress. Meanwhile, the fourth term on the LHS represents the influence of the Ampere force on the vibration.

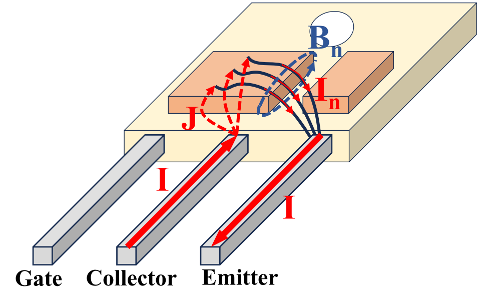

Fig. 1. TO247 package bonding wire structure and current path diagram.

B. Impact of Bond Wire Lift-Off on EMVP

IGBT devices typically use wire-bonded packaging, with high-purity aluminum bond wires for internal electrical connections. Taking the Infineon IKW75N60 T IGBT device as an example, the device contains five bond wires. Two of the bond wires are connected to the chip and the emitter, another two bond wires are connected to the reverse-parallel diodes and the emitter, and a finer bond wire is connected to the gate.

Fig. 1 shows the model of a single TO247-3 packaged IGBT device. In real operating conditions, the bond wires connected to the IGBT chip experience the highest thermal stress, making

them particularly prone to lift-off and other defects. Therefore, the model only considers the bond wires directly connected to the IGBT chip. In the packaging structure shown in Fig. 1, the collector is connected to the copper frame. When the IGBT is turned ON, the collector current flows from the pin, through the copper frame, IGBT chip, and bond wires, and then exits through the emitter pin. Given the small size of the external pins and bond wires, the internal current can be simplified to a line current model. Assuming the collector current flowing in is I. For an IGBT with N bond wires, the current I_n on each bond wire is I/N. The current density J in the copper frame and inside the chip can be solved as follows:

$$\begin{cases} \nabla \cdot J &= 0 \\ \nabla \cdot H &= 0 \\ \nabla \times J &= -\sigma\mu \frac{\partial H}{\partial t} \\ \nabla \times H &= J. \end{cases} \tag{6}$$

Since the conduction current is significantly greater than the displacement current, the effect of the displacement current on the magnetic field is neglected. According to the Biot–Savart law, the magnetic induction $d\mathbf{B}$ generated by a current element $Id\mathbf{l}$ at position $\mathbf{r}$ is given as follows:

$$d\mathbf{B} = \frac{\mu_0}{4\pi} \frac{Id\mathbf{l} \times \mathbf{r}}{|\mathbf{r}|^3}. \tag{7}$$

Therefore, the currents in the collector pin, emitter pin, and bond wires generate magnetic fields in space as follows:

$$\mathbf{B}_{\text{collector}} = \frac{\mu_0}{4\pi} \int_{C_c} \frac{Id\mathbf{l} \times \mathbf{r}}{|\mathbf{r}|^3} \tag{8}$$

$$\mathbf{B}_{\text{emitter}} = \frac{\mu_0}{4\pi} \int_{C_e} \frac{Id\mathbf{l} \times \mathbf{r}}{|\mathbf{r}|^3} \tag{9}$$

$$\mathbf{B}_{\text{bond}} = \sum_{n=1}^{N} \frac{\mu_0}{4\pi} \int_{C_{\text{bn}}} \frac{(I/N)d\mathbf{l} \times \mathbf{r}}{|\mathbf{r}|^3}. \tag{10}$$

Here, C_c, C_e, and C_{bn} represent the current flow paths of the collector pin, emitter pin, and bond wire n, respectively.

The magnetic field generated by the current density $\mathbf{J}$ within the copper frame in space can also be expressed as follows:

$$\mathbf{B}_{\text{copper}} = \frac{\mu_0}{4\pi} \int_V \frac{\mathbf{J} \times \mathbf{r}}{|\mathbf{r}|^3} dV \tag{11}$$

where V represents the volume of the copper frame. By neglecting the effects of distant current elements, the total magnetic field near the bond wires can be expressed as follows:

$$\mathbf{B} = \mathbf{B}_{\text{collector}} + \mathbf{B}_{\text{emitter}} + \mathbf{B}_{\text{bond}} + \mathbf{B}_{\text{copper}}. \tag{12}$$

Further, the Ampere force acting on the ith bond wire can be expressed as follows:

$$\mathbf{F}_n = \int_{C_{\text{bn}}} (I/N)d\mathbf{l} \times \mathbf{B}. \tag{13}$$

Temperature fluctuations result in varying degrees of thermal strain across different materials. Over time, the accumulation of stress can lead to fatigue and lift-off of the bond wires. When bond wire lift-off occurs, the current within the detached bond wire drops to zero, while the current in the remaining bond wires increases. In addition, the detached bond wire no longer generates a magnetic field, leading to a change in the overall magnetic field, which can be expressed as follows:

$$\mathbf{B}'_{\text{bond}} = \sum_{n=1}^{N'} \frac{\mu_0}{4\pi} \int_{C_n} \frac{(I/N')\, d\mathbf{l} \times \mathbf{r}}{|\mathbf{r}|^3} \tag{14}$$

Here, N' represents the number of bond wires maintaining electrical connection.

Due to the limited impact of bond wire lift-off on the currents in the collector pin, emitter pin, and copper frame, the magnetic fields generated by these two components of current are assumed to remain unchanged. At this point, the Ampere force on the ith remaining bond wire can be expressed as follows:

$$\mathbf{F}'_n = \int_{C_n} (I/N')\, d\mathbf{l} \times \mathbf{B}'. \tag{15}$$

Here

$$\mathbf{B}' = \mathbf{B}_{\text{collecter}} + \mathbf{B}_{\text{emitter}} + \mathbf{B}'_{\text{bond}} + \mathbf{B}_{\text{copper}}. \tag{16}$$

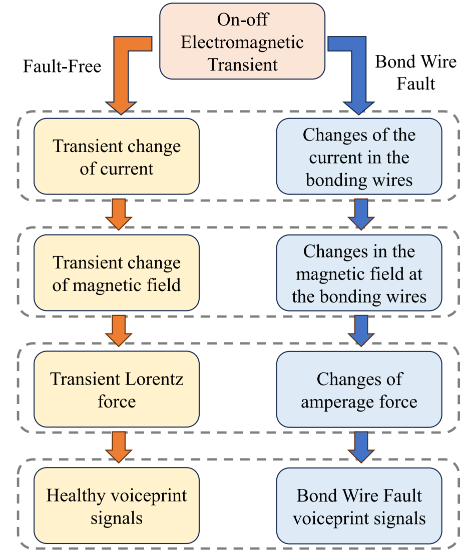

Fig. 2. Process of influence of bond wire lift-off on EMVP signal.

The mechanism of EMVP signal changes caused by bond wire lift-off failure is illustrated in Fig. 2. During the transient switching of the IGBT, the rapid variation of current causes the bond wires to experience transient ampere forces, resulting in vibrations. These vibrations propagate to the surface of the device and are captured by the AE sensors. When a bond wire lifts-off, significant changes occur in the current within each bond wire. At the same time, the magnetic field around the bond wire also changes due to the variation in current. The variation in the electromagnetic field induces changes in the EMVP signals. Theoretically, transient current changes within the copper frame and IGBT chip would also induce corresponding EMVP signals. However, since the copper frame experiences only magnetic field changes without significant current variation, its impact on the EMVP is less pronounced than that of the bond wire.

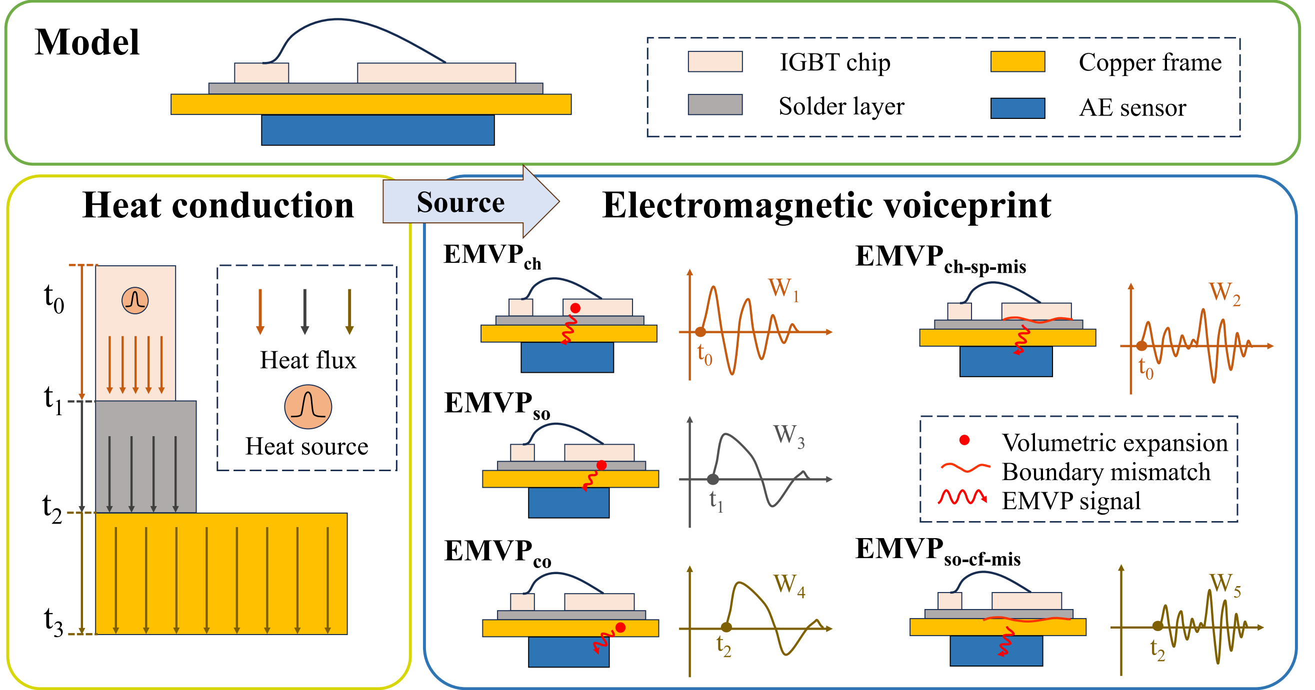

Fig. 3. Mechanism diagram of the impact of heat conduction in the packaging structure on EMVP signals. Thermal pulse and thermal expansion of multilayer materials caused by heat transfer effect together generate EMVP signals.

C. Impact of Solder Layer Defects on EMVP

Previous studies have highlighted the mechanism of EMVP generation due to the thermal expansion effect in IGBT chips [29]. This article will further elaborate on the crucial role of heat conduction in the packaging structure in the generation of EMVP. Fig. 3 illustrates the process by which the thermal expansion effect leads to EMVP signals. The IGBT device consists of multiple material layers, with the copper frame and IGBT chip tightly bonded together by a solder layer. The heat generated by the IGBT chip is conducted through the chip-solder-copper path. In the IGBT chip layer, a volumetric heat source is generated by the electromagnetic thermal effect. Assuming uniform current distribution within the chip, this can be expressed as follows:

$$Q_{\mathrm{v}} = \frac{U_{\mathrm{c\,e}} \cdot I_{\mathrm{c}}}{V} \tag{17}$$

where $U_{\mathrm{c\,e}}$ is the collector-emitter voltage, I_{c} is the collector current, and V is the chip volume. The IGBT chip layer satisfies the heat conduction equation as follows:

$$\rho_{\mathrm{ch}} c_{\mathrm{ch}} \dot{T}^{\mathrm{ch}} = k_{\mathrm{ch}} T_{ii}^{\mathrm{ch}} + Q_{\mathrm{v}} \tag{18}$$

where ρ_{ch}, c_{ch}, and k_{ch} are the density, specific heat capacity, and thermal conductivity of the chip, respectively. T represents the temperature field within the chip. If the IGBT chip generates a thermal pulse at time t, it will directly cause a temperature rise in the chip. The chip's thermal expansion effect will lead to the EMVP signal of P1 part in Fig. 3 as follows:

$$\mathrm{EMVP}_{\mathrm{ch}} = W_1\left(t - t_0\right) u\left(t - t_0\right) \tag{19}$$

where $W_1(t - t_0)$ represents the EMVP signal generated by the chip, and $u(t - t_0)$ represents the step signal.

As the temperature of the chip layer increases, a temperature difference exists at the interface between the chip layer and the solder layer. In addition, the differing thermal expansion coefficients of the chip and solder layer cause a significant thermal stress concentration at the interface. This mismatch at the boundary becomes a new source of EMVP emission. Since the chip temperature rises almost simultaneously, the EMVP signal shown in the P2 part also starts at time t_0 and is expressed as follows:

$$\mathrm{EMVP}_{\mathrm{ch-sp-mis}} = W_2\left(t - t_0\right) u\left(t - t_0\right). \tag{20}$$

In the solder layer, heat conduction follows:

$$\rho_{\mathrm{so}} c_{\mathrm{so}} \dot{T}^{\mathrm{so}} = k_{\mathrm{so}} T_{ii}^{\mathrm{so}} \tag{21}$$

Here, the superscript so denotes the solder layer. Due to the time required for heat conduction through the solder and chip, it is assumed that a significant impact on the temperature of the solder layer occurs after a time t_1. Therefore, the EMVP signal generated by the thermal expansion effect in the solder layer, shown in the P3 part, can be expressed as follows:

$$\mathrm{EMVP}_{\mathrm{so}} = W_3\left(t - t_1\right) u(t - t_1). \tag{22}$$

Subsequently, heat is conducted through the solder layer, and at time t_2, it has a significant impact on the average temperature of the copper frame. Therefore, the EMVP signal generated by the thermal expansion effect in the copper frame, shown in the P4 part, can be expressed as follows:

$$\mathrm{EMVP}_{\mathrm{co}} = W_4\left(t - t_2\right) u(t - t_2). \tag{23}$$

At the same time, the temperature changes in the solder layer and copper frame will also cause thermal stress concentration

near their contact interface, generating the EMVP signal due to the mismatch in thermal expansion coefficients between the solder layer and the copper frame, as shown in the P5 part. This can be expressed as follows:

$$\mathrm{EMVP}_{\mathrm{so-cf-mis}} = W_5\left(t - t_2\right) u(t - t_2). \tag{24}$$

It is important to note that the generation of all EMVP signals is closely related to temperature changes, but each exhibits different characteristics. W_1 shows an initial pulse followed by attenuation due to the pulse heat source present when the IGBT turns ON and OFF. W_3 and W_4 exhibit lower frequency variations as the thermal conduction process within the materials acts over a longer time scale. W_2 and W_5 are closely related to the temperature changes in the materials on both sides, as well as their thermal expansion coefficients. The more intense the temperature change, the greater the variation in the thermal expansion dimensions of the materials over time. This results in repeated stretching or compressing stresses on the materials, generating EMVP signals with higher frequency and broader spectral range. The EMVP signal captured by the sensor is the superposition of multiple EMVP signals. The final EMVP signal can be expressed as follows:

$$\mathrm{EMVP} = \sum_i \mathrm{EMVP}_i = \sum_i W_i\left(t - t_i\right) u(t - t_i). \tag{25}$$

Another point to note is that the EMVP generated by the thermal conduction process differs in time scale from that produced by the ampere force. The EMVP induced by the ampere force is based on transient electromagnetic forces, after which the device enters a state of free vibration, with the total energy continuously decaying. In contrast, the thermal conduction process occurs more slowly, leading to the continuous generation of new EMVP signals during heat transfer. As a result, the overall duration of the EMVP is longer, and there may be periods where the EMVP energy increases.

The impact of solder layer defects on EMVP signal can be summarized in Fig. 4. If defects or degradation occur in the solder layer, it will lead to an increase in thermal resistance and heat capacity, affecting the heat conduction process. This results in changes to the temperature-time curves of the multilayer materials, which in turn affects the intensity of EMVP emission. In addition, the increase in heat capacity alters the heat transfer rate, changing the timing of the EMVP signal. Furthermore, degradation of the solder layer can alter the properties of the contact interface, which in turn affects the characteristics of the EMVP emission source, leading to differences in frequency. The frequency change phenomenon has been demonstrated in previous studies [25], [26]. Finally, defects or degradation in the solder layer will affect the propagation of the EMVP signal, resulting in an increase in acoustic impedance. Overall, in the presence of solder layer defects, the EMVP signal becomes:

$$\begin{aligned}\mathrm{EMVP}' &= \sum_i \mathrm{EMVP}'_i \\ &= \sum_i W'_i\left(t - t_i - t'_i\right) u\left(t - t_i - t'_i\right). \end{aligned} \tag{26}$$

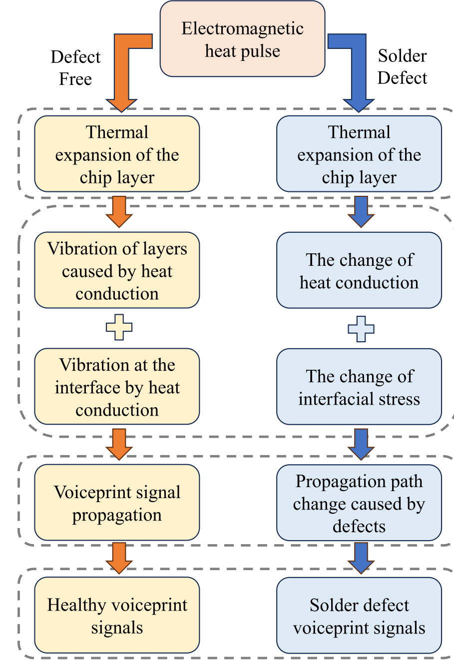

Fig. 4. Process of influence of package structure heat conduction on EMVP signal.

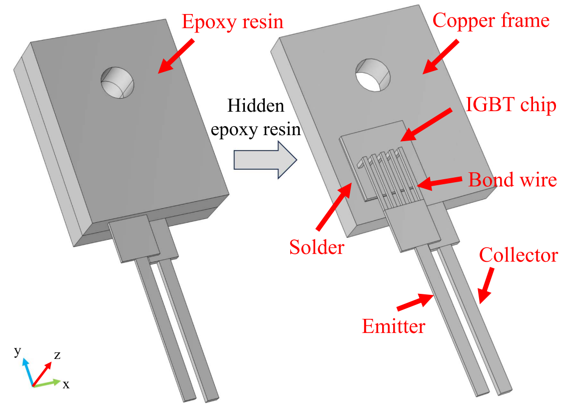

Fig. 5. Simulation model of bond wire lift-off impact.

Here, W'_i is the EMVP signal affected by interface and propagation characteristic changes, t'_i is the signal time delay caused by changes in the heat capacity of solder layer.

III. Finite Element Simulation Model

A. Bond Wire Lift-Off Impact on EMVP Signal Model

To simulate the impact of bond wire lift-off on EMVP signals, a multiphysics finite element model coupling electromagnetic fields and solid mechanics, as shown in Fig. 5, is built. The IGBT device includes a copper frame, solder layer, IGBT chip, epoxy resin package, collector, emitter, and multiple bond wires connected to the emitter. Since the bond wires are enclosed within the epoxy resin package, the model includes the epoxy resin package as part of the simulation. The *Z*-axis is set to be perpendicular to the surface of the package. Considering that the magnetic field distribution of the current is primarily

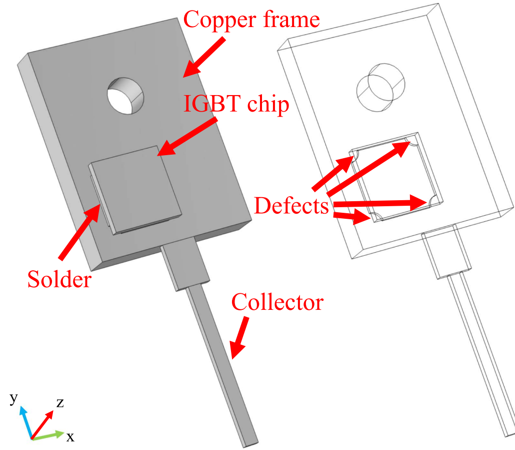

Fig. 6. Simulation model of solder defects impact.

concentrated in the Z-direction, the size of the air domain is set to exceed the IGBT model size by at least five times along the Z-axis. The collector and emitter pins are extended to the air domain boundary, adding terminal and grounding boundary conditions. In addition, in the solid mechanics field, the bottom of the collector and emitter pins is set as a fixed constraint boundary. A peak current of 40 A is injected from the collector, and the current waveform is represented as follows:

$$\begin{cases} 0.67t & 0 \leq t \leq 60 \\ 0.1t^2 - 16t + 640 & 60 \leq t \leq 80 \\ 0 & t > 80. \end{cases} \tag{27}$$

The unit for t is microseconds (μs). Although IGBT devices of typical TO247 packages generally have fewer bond wires, the model includes up to five bond wires to better illustrate the impact of bond wire lift-off on EMVP signals. The bond wire material is set to aluminum. The internal body load of the device is calculated using the Lorentz force effect. Rayleigh damping is incorporated in the model to simulate the absorption and attenuation effects of the EMVP signal as it propagates through the solid. The parameteric scan function is used to gradually reduce the number of bond wires and calculate the EMVP signal of the device for different numbers of bond wires. The measurement point is selected on the epoxy resin surface.

B. Solder Defects Impact on EMVP Signal Model

To simulate the impact of solder layer defects on EMVP signals, a multiphysics finite element model coupling solid heat transfer and solid mechanics is developed, as shown in Fig. 6. In contrast to Fig. 5, the emitter pin and bond wire are excluded, as their structures have minimal impact on the study of solder layer defects. In addition, the epoxy resin layer is removed, as its low thermal conductivity means that the heat generated by the IGBT chip mainly propagates through the solder layer to the copper frame.

For the boundary conditions, a high convection heat transfer coefficient is applied to the surfaces in contact with the device's metal structure and air, while other surfaces are assigned a lower convection heat transfer coefficient. The heat source is located within the IGBT chip, represented by a Gaussian pulse waveform with an amplitude of 20 000 W and a duration of 0.5 μs.

A circular defect is set at the edge of the solder layer to simulate delamination. The severity of the defect is controlled by the void ratio, which is defined as follows:

$$R_h = \frac{S_h}{S_s} \tag{28}$$

where S_h is the void area and S_s is the total area of the solder layer. The void rates are set to 6%, 12%, 18%, 24%, and 30% through a parameteric scan. EMVP signals are collected at the center of the IGBT copper frame surface.

C. Simulation Results of Bond Wire Lift-Off Impact on EMVP

Fig. 7 shows the Von Mises stress distribution contour of the IGBT device with varying numbers of bond wires. It is observed that the stress is primarily concentrated on the bond wires due to the higher current density in these areas, resulting in greater ampere forces. When more bond wires are present, the current and magnetic field distributions are more uniform, leading to lower stress on both the bond wires and other parts of the IGBT device. Conversely, as the number of bond wires decreases, both the current and magnetic field become more concentrated, causing a gradual increase in the peak Von Mises stress on the bond wires.

Fig. 8 shows the EMVP signal waveforms for different numbers of bond wires. It can be observed that as the number of bond wires decreases, the amplitude of the EMVP signals increases. Although a single bond wire no longer generates EMVP signals after it lifts off due to the absence of ampere forces, the redistribution of current and magnetic fields caused by the lift-off increases the total stress on the remaining bond wires, thereby enhancing the EMVP signal.

Fig. 9 shows the variation of the peak-to-peak value of the EMVP signal with the number of bond wires. The figure shows that as the number of bond wires decreases, the peak-to-peak value of the EMVP signal exhibit a faster growth trend. From the simulation results, it can be seen that compared to early bond wire failures, the EMVP signal is more sensitive to severe bond wire lift-off.

D. Simulation Results of Solder Defects Impact on EMVP

As illustrated in Fig. 10, the simulated EMVP waveform of an IGBT device with a 30% void ratio is used as an example for explanation. The waveform is divided into two parts in the time domain, namely, S1 and S2. The boundaries of S1 and S2 are defined as the first local minimum of the peak envelope of the EMVP signal after the IGBT device is turned OFF. Specifically, the local peak curve is first used to identify the peak points of the EMVP. Then, spline interpolation is applied to obtain the peak envelope, and finally, the first local minimum of the peak envelope after the IGBT device is turned OFF is selected. From the overall characteristics of the waveform, the thermal expansion waveform exhibits characteristics distinct from those under the influence of ampere force. For the EMVP signals generated by ampere force, the waveform shows a decaying

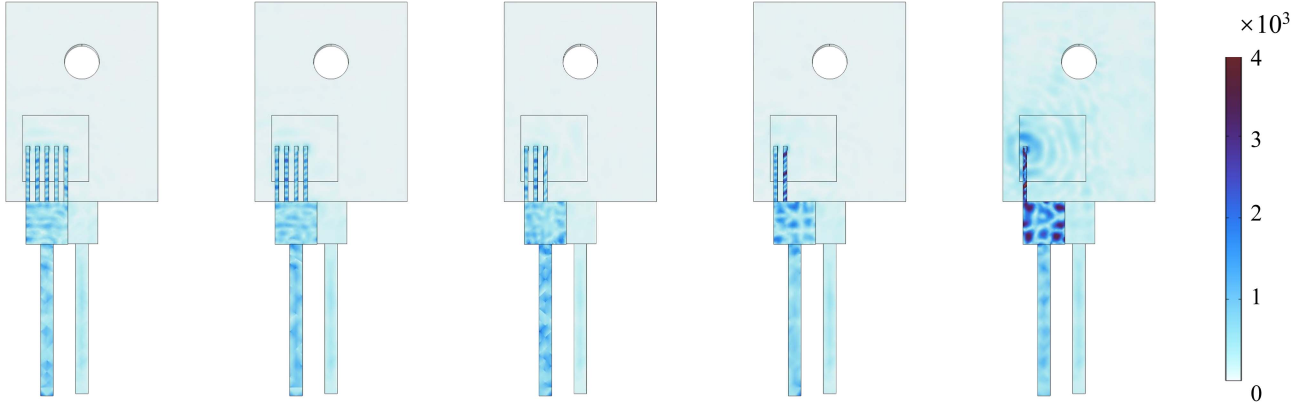

Fig. 7. Stress nephogram with different number of bonding wires.

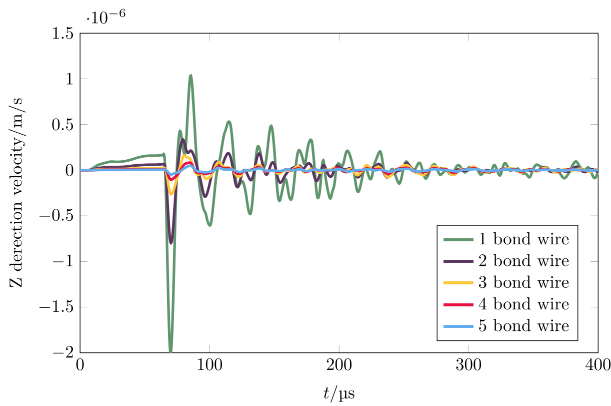

Fig. 8. Waveform of EMVP signal with different number of bond wires.

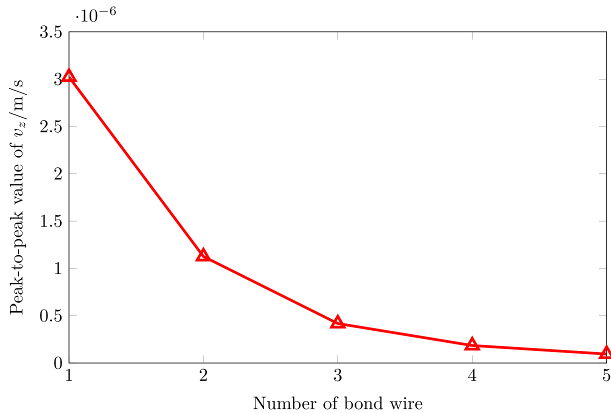

Fig. 9. EMVP signal peak to peak value with different number of bond wires.

trend. For the thermal expansion waveform, an initial decay of the thermal expansion waveform is observed within the S1 time region. However, in the S2 time region, new generated EMVP signals are continuously detected. The boundaries of S1 and S2 characterize the point at which the initial EMVP has attenuated to a certain degree, but the generation of new EMVP has not yet significantly occurred. As described in the theoretical model, the ampere force is a transient excitation that disappears after a short period. Thermal expansion, however, involves both heat generation and heat transfer processes. The

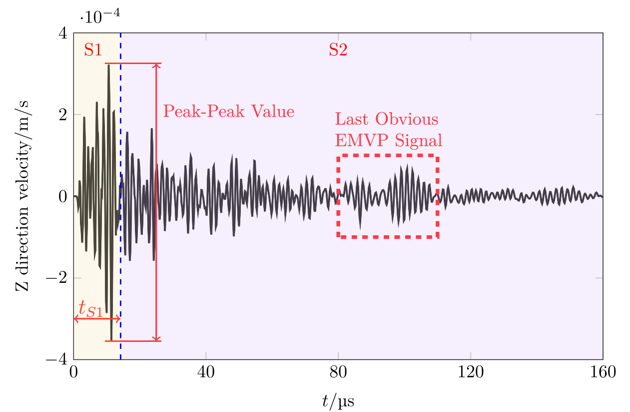

Fig. 10. Waveform of EMVP signal with 30% void ratio. In the S1 time region, the EMVP signal is mainly generated by heat pulse. In S2 time region, the EMVP signal is mainly generated by heat transfer process. After the last obvious EMVP signal, the heat transfer tends to flatten out and no longer produces significant EMVP signal.

initial thermal expansion displays transient characteristics, but subsequent EMVP emissions continue due to heat transfer. The time scale of the heat transfer process is longer than that of the transient heat source excitation during switching, leading to the phenomenon of initial waveform decay followed by the emergence of new signals.

To illustrate the impact of solder defects on the waveform, the initial relative peak–peak value, relative S1 time region energy and the voiceprint energy dominance time are extracted as features. The relative peak–peak value and relative S1 time region energy is employed to represent the effect of pulsed electromagnetic heat within the chip and is defined as follows:

$$\mathrm{REP}_i = \frac{P_i^{\mathrm{peak}}}{P_{0.06}^{\mathrm{peak}}} \tag{29}$$

$$\mathrm{REE}_i = \frac{E_i^{S1}}{E_{0.06}^{S1}} \tag{30}$$

Here, P_i is used to represent the EMVP signal of an IGBT device with a void ratio of i. P_i^{peak} and E_i^{S1} is the peak–peak value and S1 time region energy of the waveform with different void ratios. $P_{0.06}^{\mathrm{peak}}$ and $E_{0.06}^{S1}$ is the peak–peak value and S1 time region energy

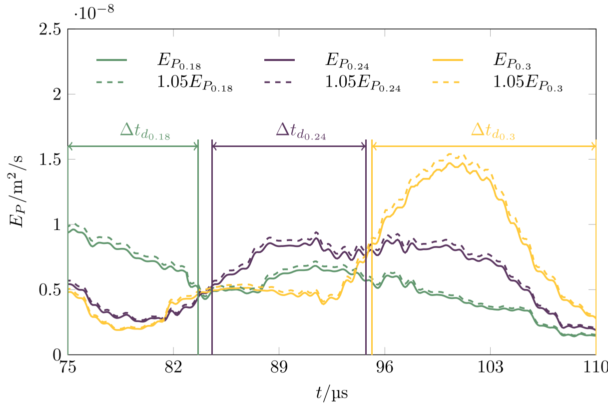

Fig. 11. EMVP energy curve and the definition of energy dominance time $\triangle t_d$ at void ratios of 0.18, 0.24, and 0.3.

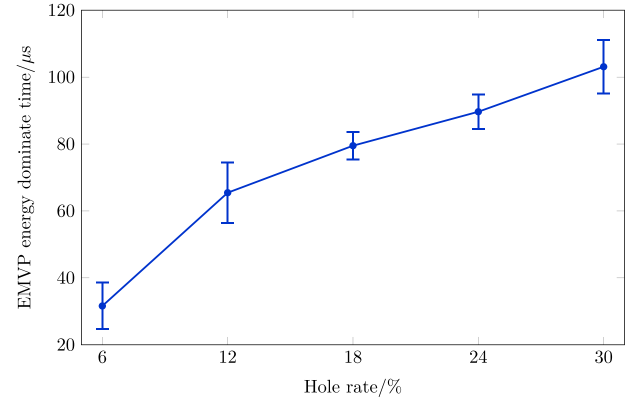

Fig. 12. EMVP energy dominance time with different void ratios. Short blue lines indicate time start and end.

TABLE I
RELATIVE REP AND REE WITH DIFFERENT VOID RATIOS

Void Ratio/%	6	12	18	24	30
REP	1.000	0.984	0.980	0.999	1.007
REE	1.000	0.981	0.976	0.994	1.003

of the waveform with a 6% void ratio. Here, S1 region energy is expressed as follows:

$$E_i^{S1} = \int_{t_{S1}} [P_i(t)]^2 dt \tag{31}$$

As shown in Fig. 10, t_{S1} is the duration of S1 stage. The EMVP energy dominance time $\triangle t_{d_i}$ is defined as follows:

$$E_{P_i}(t) > 1.05 \cdot E_{P_j}(t) \quad \forall i \neq j, \quad t \in \Delta t_{d_i}. \tag{32}$$

Here, $E_P(t)$ is the energy which is defined as follows:

$$E_{P_i}(t_0) = \int_{t_0-\Delta t_w/2}^{t_0+\Delta t_w/2} [P_i(t)]^2 dt \tag{33}$$

Here, Δt_w is the window size. Fig. 11 shows the EMVP energy curves for void ratios of 18%, 24%, and 30% with a time window length of 100. The energy dominance times for the three cases are labeled based on the definition. The voiceprint energy dominance time represents the time duration during which the energy of the EMVP signal P_i exceeds 5% of the energy of the others. It characterizes the effect of solder layer defects on the release time of the EMVP.

Table I shows the relative peak-peak value and relative S1 time region energy with different void ratios. The results indicate that the differences in these two features are minimal, with the maximum differences being 0.98 and 0.976, respectively. This is because, during the S1 stage, the thermal pulse has just been generated, and significant heat transfer has not yet occurred. Consequently, the temperature distribution remains similar under the same thermal pulse, resulting in comparable initial EMVP energy.

Fig. 12 shows the energy dominance time for different void ratios. The figure indicates the time range and the central time point of the dominance time for each void ratio. It can be observed that as the void ratio increases, the central time point shifts progressively later. This indicates that an increase in the void ratio affects the thermal capacity and thermal resistance, leading to a delay in the generation of the EMVP. The result is consistent with the theoretical analysis, which suggests that the slowed heat transfer process results in a time delay in the EMVP.

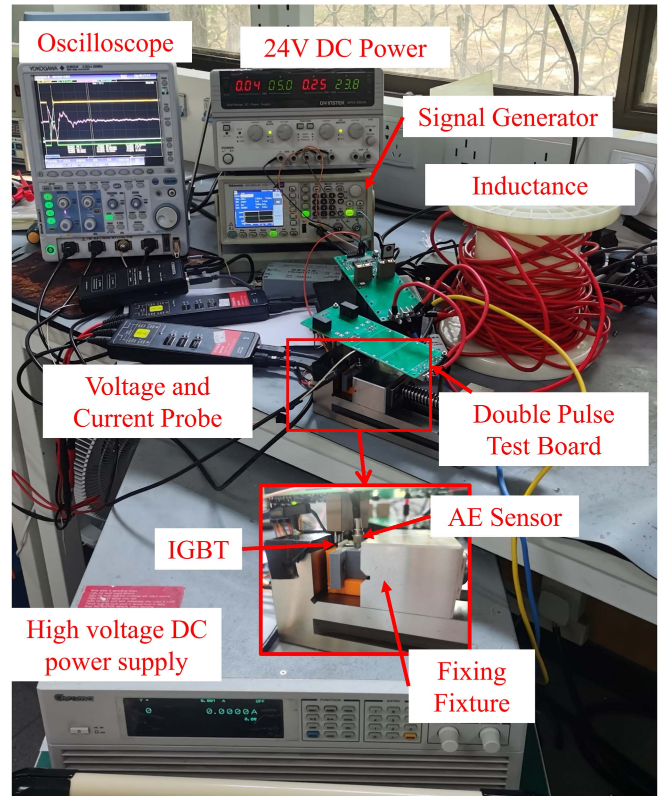

Fig. 13. Experimental platform.

IV. EXPERIMENT SETUP AND RESULTS

A. Experiment Platform

The experiment platform shown in Fig. 13 was constructed to collect EMVP signals from IGBT devices. The platform includes a dc power supply, signal generator, AE probe, mounting fixture, oscilloscope, wound inductor, and double-pulse test board. The AE probe is the G150, with a frequency range of 40 kHz to

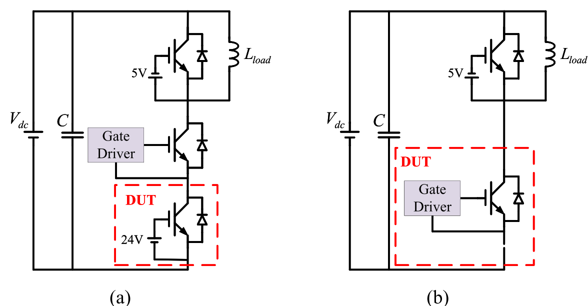

Fig. 14. Experimental circuit diagram. (a) Ampere force test circuit diagram. (b) Thermal expansion test circuit diagram.

400 kHz. The AE probe is connected to a preamplifier and a filter, with the preamplifier having a gain of 40 dB and a filter frequency range of 20 kHz to 1.2 MHz. The oscilloscope is YOKOGAWA DLM2034 with a sampling rate of 250 MHz. The wound inductor is made from copper coils, and its inductance value is calibrated using an impedance tester before each test. The current probe used is the CP9012S, with a sensitivity of 50 mV/A. The voltage probe is a differential high-voltage probe with a 500 attenuation factor. Preliminary tests identified three major factors affecting the measurement of IGBT EMVPs: the fixed position of the AE probe, the contact tightness between the AE probe and the IGBT, and circuit board vibrations. To eliminate the influence of these factors, a 3-D-printed mold was used to ensure a consistent relative position between the probe and the IGBT. In addition, a high-precision mounting fixture, combined with a torque wrench, was used to maintain consistent contact tightness between the AE probe and the IGBT. Finally, copper standoffs were used to secure the circuit board to the fixture base, minimizing the impact of vibrations on EMVP signal collection. Preliminary tests were conducted to ensure that these three factors do not affect the experimental results. The experiment was based on the double-pulse test circuit shown in Fig. 14. To prevent the interaction between ampere force and thermal expansion effects, the circuit shown in Fig. 14(a) was used to extract the EMVP generated by ampere force. In the circuit, an additional controlled switch is added to the lower bridge arm, while the device under test remains in an ON state, ensuring that the thermal pulse of the device under test is nearly zero. When investigating the impact of solder layer defects on the EMVP signal, circuit Fig. 14(b) was used. By increasing the turn-ON and turn-OFF resistance, the influence of the thermal pulse was enhanced, ensuring that the EMVP energy due to thermal pulses was at least ten times greater than that from the ampere force. In the experiment, the bus voltage was set as 500 V, and the current at the turn-OFF moment was 40 A. Practical tests showed that due to the relatively low turn-OFF current, the EMVP caused by the ampere force was minimal. Therefore, in studies focusing on ampere force, the gain of the preamplifier was increased to 60 dB.

B. IGBT Device Processing

The IGBT used in the experiment is TO-247 package, with a rated voltage of 600 V, a rated current of 75 A, and an operating junction temperature 175 °C. Fig. 15 illustrates the process of device preparation for ampere force investigation. The IGBT contains two bond wires internally, so a set of three IGBT devices was used for comparative testing. The device's epoxy resin layer was selectively heated with a laser until a portion was exposed, revealing the two bond wires connected to the IGBT chip. One of the two bond wires was then cut sequentially. An additional IGBT device served as a control, with its bond wires left intact. Finally, the exposed section of the epoxy resin layer was resealed with fresh epoxy resin. Once the newly applied epoxy had hardened, it was lightly polished to ensure a smooth surface. It was essential to carefully monitor the depth of laser removal to avoid reaching the IGBT chip

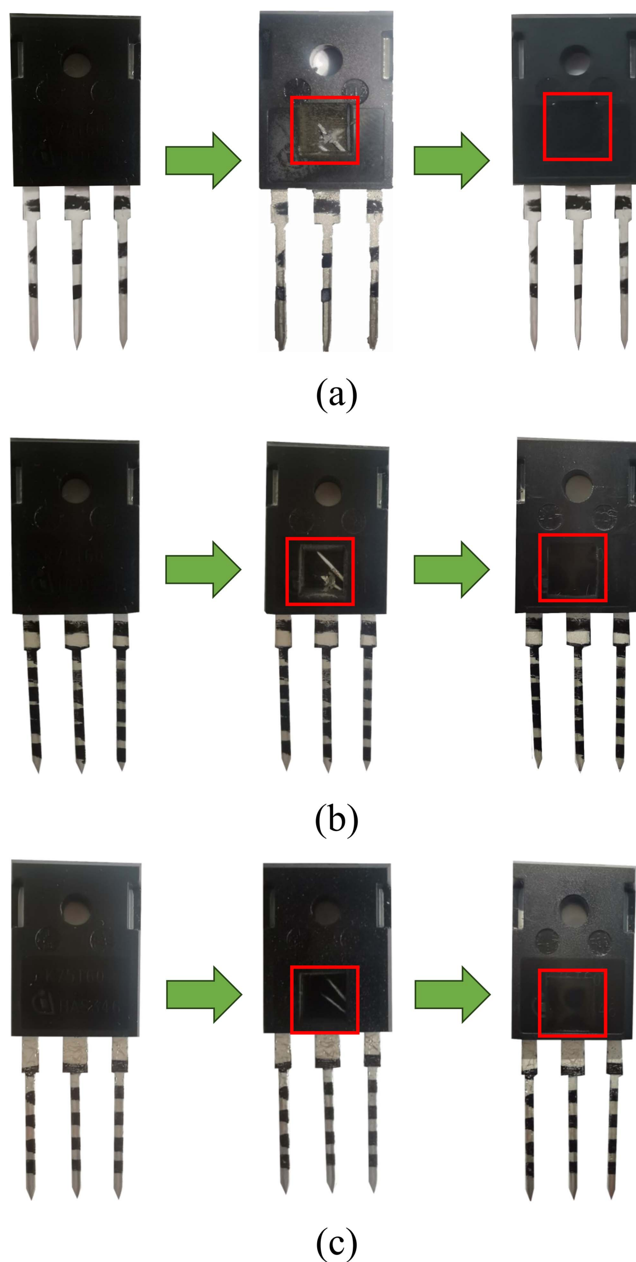

Fig. 15. TO247 package bonding wire processing. (a) Cut the central bond wire. (b) Cut the side bond wire. (c) Control group without cutting bond wire.

layer, which could lead to device failure. Throughout the removal process, an infrared thermometer was used to continuously track the surface temperature of the device, ensuring it stayed below the rated junction temperature. If needed, the laser was turned OFF to allow the device to cool. To ensure the reliability of the results, three additional devices were treated in the same way as a repeat control group. The experimental and repeat control groups were labeled G1 and G2, respectively.

For the thermal expansion EMVP experiments, the devices underwent accelerated aging tests through thermal cycling. Each cycle lasted 1 h and included 25 min at a high temperature of 125 °C, 25 min at a low temperature of −40 °C, and a 10 min transition phase. The devices were subjected to a total of 1000 hours of thermal cycling, which induced defects such as delamination and voids in the solder layer. The EMVP signals were measured at different stages: unaged, and after 250, 500, 750, and 1000 hours of aging. It is worth noting that thermal cycling aging may also cause defects in the bond wires. However, since bond wire defects have an insignificant impact on heat transfer, their effect on the experimental results is minimal.

C. Experimental Result of Influence of Bond Wire Lift-Off

Due to the fast response and short duration of the ampere force, EMVP signals were collected around the IGBT turn-ON and turn-OFF time points. Fig. 16(b) and (c) shows the EMVP signals for group G1 and G2. Fig. 16(a) is the current of the collector. The dashed lines in the figures indicate the status of the controlled IGBT device in the lower bridge.

Each switching action of the device generates electromagnetic noise that couples into the AE sensor, resulting in a pulse followed by a period of high-frequency oscillation. The low-frequency components in the EMVP waveforms reflect the vibration characteristics of the device caused by the ampere force. At 2 μs, the controlled IGBT device turns ON, causing the inductor current to rise. With small current magnitude and rate of change, the ampere force is minimal, and the signal is mainly composed of electromagnetic noise coupled into the sensor. At 13 μs, the controlled IGBT device turns OFF with a current of 40 A, generating a more significant electromagnetic coupling pulse spike, followed by noticeable differences in the low-frequency signal amplitude. The EMVP amplitude of devices with intact bond wires is lower than that of faulty devices. At 18 μs, the controlled IGBT device turns ON again with a current of 40 A. The low-frequency vibrations in the EMVP signals show a more pronounced amplitude difference between devices before and after lift-off. Furthermore, the vibration amplitude of device with cut edge bond wire is higher than the cut center bond wires, as the center bond wire is closer to the AE sensor, making its vibration more easily detectable.

Fig. 17 shows the frequency spectrum of the EMVP waveform. It can be observed that within the frequency range of 100 to 120 kHz, there are noticeable differences in the EMVP signal amplitudes under different bond wire conditions. A decrease in the number of bond wires increases the EMVP intensity, which aligns with the simulation results. Furthermore, the spectral characteristics of the experimental group (G1) and the control

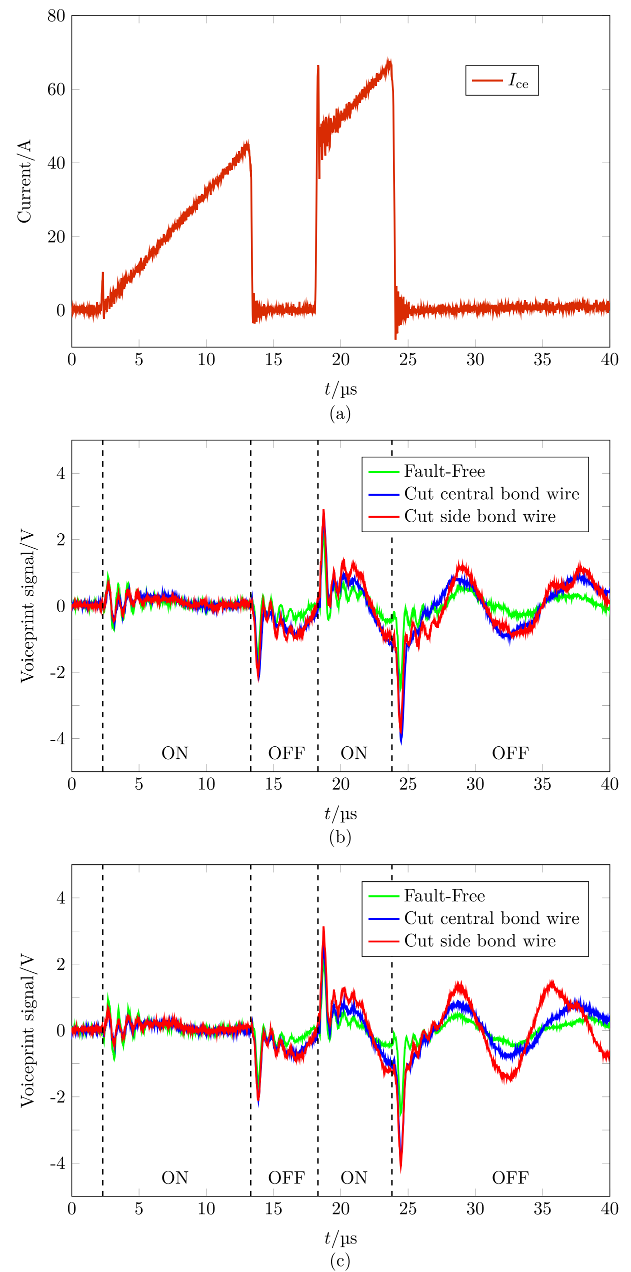

Fig. 16. EMVP signals under different bond wire conditions. (a) Current of the collector. (b) EMVP of group G1. (c) EMVP of group G2.

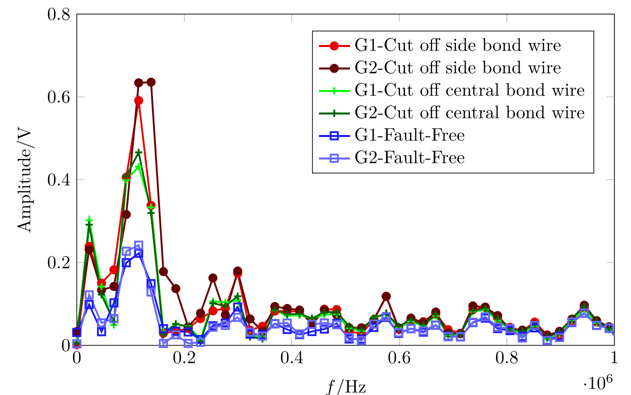

Fig. 17. Frequency spectrum of the EMVP waveform.

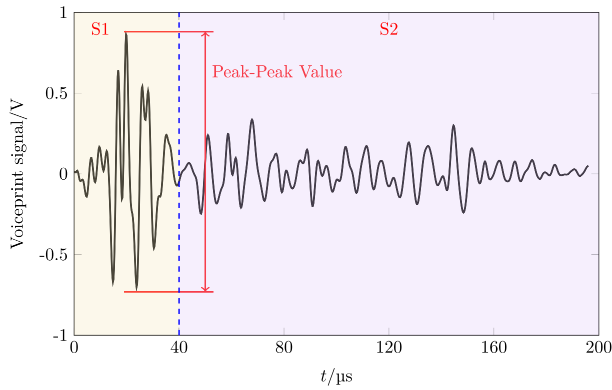

Fig. 18. EMVP signals measured by 1000 h aging time device. In the S1 time region, the EMVP signal is mainly generated by heat pulse. In S2 time region, the EMVP signal is mainly generated by heat transfer process.

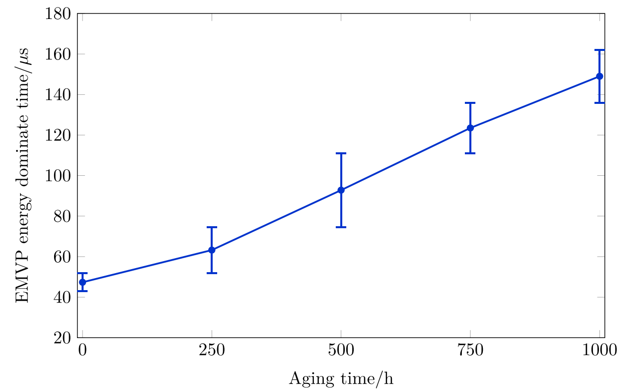

Fig. 19. EMVP energy dominance time with different aging time. Short blue lines indicate time start and end.

TABLE II
EMVP ENERGY DOMINANCE TIME WITH DIFFERENT VOID RATIOS

Aging Time/h	0	250	500	750	1000
REP	1.000	0.944	0.961	0.949	0.834
REE	1.000	0.967	0.973	0.958	0.836

group (G2) show minimal differences, indicating that the process of removing the epoxy resin packaging and reseal has little effect on the IGBT's EMVP characteristics.

The influence of different positions of the failed bond line on the EMVP signal can also be observed from the spectrum. After the failure bond wire is disconnected, the amplitude of the EMVP spectrum increases when the intact bond wire is positioned closer to the AE sensor. This is because the AE sensor is located at the bottom of the central bond wire, causing the EMVP generated by the central bond wire to experience less attenuation as it propagates toward the sensor. In addition, the energy distribution at different frequency points in the spectrum shows distinct variations. This is due to the close relationship between EMVP propagation and solid boundary conditions. EMVP generated by bond wires located at the edges is more likely to be affected by the boundaries of the IGBT chip, such as stress concentration at the edges.

D. Experimental Result of Influence of Solder Defects

Fig. 18 shows the EMVP signals measured at 1000 h thermal cycling aging time. Over a longer time scale in S2 time region, EMVP signals continuously generate, exhibiting characteristics similar to the simulated waveforms. Within the first 40 μs, the initial EMVP energy is high, followed by a decay. This part of the EMVP is caused by the thermal expansion of the chip and the stress at the chip-solder interface, with the temperature change being most pronounced during this period, resulting in a larger amplitude. Between 40 μs and 160 μs, the previously decaying EMVP signal shows an increase in energy, which persists for a period, indicating the emission of a EMVP signal. After 160 μs, temperature fluctuations across all layers stabilize, and the EMVP weakens significantly.

Table II displays the first relative peak–peak values and S1 time region energy at different aging stages. The maximum difference is 0.834 and 0.836, respectively. Both observed after 1000 h of aging. This is likely due to delamination and voids in the solder layer, which alter the chip-solder interface properties, resulting in EMVP signals with varying amplitudes. Overall, the peak–peak value and energy differences across aging stages are relatively small, which aligns with the simulation results.

Fig. 19 illustrates the EMVP enegy dominant time curve, showing a noticeable trend of the central time point shifting backward. In combination with Fig. 18, it can be observed that during the dominant time period of the 1000 h aged device, there is an increase in the EMVP amplitude, corresponding to the final significant EMVP signal generated by the heat transfer process. As the aging time increases, the dominant time gradually shifts later. The results are consistent with the simulation data, confirming the validity of the proposed theory and simulation model.

V. DISCUSSION

A. Limitations of the Mechanism Model

The theory proposed in this article is a possible explanation for the effect of package health status changes on EMVP signal. Unfortunately, due to the tight integration of the IGBT package, it is difficult to isolate and observe the impact of each component of the packaging structure in the research. For example, the EMVP signal caused by heat conduction is the superposition of multiple EMVP emission sources that are hard to be separated.

Although the finite element method provides valuable insights into the propagation of the EMVP within the device, it cannot accurately model actual defects. Instead, it serves as an approximation of the real-world conditions. In addition, previous studies have shown that factors such as bus voltage, turn-OFF current, and AE sensor placement can also influence the EMVP signals of IGBT devices. For instance, changes in sensor position can affect the propagation path of the EMVP, resulting in the reception of different signals. AE sensors located farther from the IGBT chip will decrease the sensitivity of the EMVP monitoring method. Since this article primarily investigates the impact of defects on the EMVP, other influencing factors are not considered in detail. Therefore, the study is conducted under conditions that are nearly identical, with the exception of varying defect states.

Nevertheless, the study provides a potential explanation for the impact of solder aging on EMVP signals, as phenomena such as the hypothesized delay in dominant time align with experimental observations.

B. Effects of Different TO247 Packages

The proposed theory can serve as a foundation for health monitoring of IGBT packaging. It is important to note that the IGBT device used in this study represents a typical TO247 package. In practice, TO247 packages from different manufacturers may have distinct characteristics, such as variations in the positioning of the IGBT chip within the package. To optimize monitoring sensitivity, the position of the AE sensor should be adjusted based on the location of the IGBT chip, minimizing the distance between the EMVP and the sensor. In addition, the IGBT chip is often integrated with a antiparallel diode within the same package. However, the presence of the antiparallel diode does not affect the performance of the EMVP monitoring method. In the case of bond wire failures, the antiparallel diode does not significantly impact the transient current variations during IGBT chip switching. Similarly, for soldering defects, since the switching loss of the antiparallel diode is much lower than that of the IGBT chip, it does not notably influence the EMVP generated by thermal expansion effects.

C. Extended Applicability of the Mechanism Model

In addition to the IGBT device used in this article, the proposed mechanism models are also applicable to welded MOSFETs, IGBT modules, and other power electronic devices. The packaging of IGBT modules differs from that of TO247 devices due to its more complex layered structure, which includes additional solder and ceramic layers. This configuration introduces distinct characteristics in the generation and propagation of EMVP. However, this structural change does not affect the tight connection between the packaging layers, so it does not have a greater impact on the generation and propagation of EMVP. The mechanisms by which the defects discussed in this article affect the EMVP characteristics are still applicable to IGBT modules. In addition, an IGBT module with multiple semiconductor chips may lead to some EMVP signal aliasing. Therefore, the sensor position should be selected to maximize the energy contribution of the EMVP signal from the chip being monitored. Moreover, since the EMVP signals from different chips may exhibit phase differences, employing a multisensor joint analysis can effectively differentiate the signals from each chip. By analyzing the current and heat transfer paths of different packaging structures, the EMVP signals affected by defects can be further derived and simulated, providing corresponding health monitoring methods.

VI. Conclusion

This article focuses on IGBT devices and investigates the influence mechanism of the IGBT package health status on the EMVP signals. It lays the foundation for the development of reliability assessment metrics and methods for power electronic devices based on EMVP monitoring. The main contributions of this article are as follows:

1) For the two typical reliability issues of IGBT devices, bond wire lift-off and solder layer defects, EMVP emission theoretical models based on ampere force and heat transfer processes were proposed, explaining the influence mechanism of the device package health status on the signals;
2) A finite element simulation model coupling electromagnetic transients and solid mechanics was established based on the ampere force EMVP emission theory. The results showed that the peak-to-peak value of the EMVP increased as the number of bond wires decreased;
3) Based on the heat transfer process EMVP emission theory, a finite element simulation model coupling solid heat transfer and solid mechanics was established to investigate the EMVP signals of IGBT devices under different solder layer defects. The phenomena of the dominate time delay with increasing aging were discussed;
4) By processing bond wire lift-off fault and solder aging defects, experiments were conducted to measure the EMVP signals in IGBT devices. The experimental results were consistent with the simulations, confirming the accuracy of the theoretical and simulation models.

The EMVP based health monitoring method for power electronic devices offers considerable potential for engineering applications, with power converters serving as a typical use case. Since EMVP monitoring is a noninvasive technique, compact AE sensor probes can be easily positioned near the device under observation. Although various semiconductor devices and inductors within the power converter generate EMVP signals, these signals experience significant attenuation in complex structures, resulting in minimal interference between signals from devices located at different positions. For spatial electromagnetic noise or other potential coupling noise sources, the rich features contained within the signal waveform can be leveraged to separate health condition features through methods such as feature extraction and intelligent denoising. In comparison to traditional static electrical parameter monitoring, EMVP signals contain richer information. Compared to dynamic electrical parameter monitoring methods, EMVP requires a lower sampling rate, making it more cost-effective. By deploying multiple AE probes within the power converter, an array can be easily formed, allowing for a comprehensive assessment of the overall system reliability of the power converter. And in the future, EMVP signal acquisition sensors with smaller sizes, enhanced anti-interference capabilities, and improved electromagnetic compatibility will significantly improve the effectiveness and broaden the applicability of EMVP-based condition monitoring methods in engineering.

To better validate the mechanisms, simulations, and experiments in this study were designed to make one factor's influence much larger than the other. However, in practical conditions, both factors are often coupled. Under different operating conditions, the intensity ratio of the EMVP generated by ampere force and heat transfer varies. For instance, when the switching speed is fast, causing a large current rate of change but minimal chip thermal power loss, the EMVP generated by ampere force is

more easily detected. On the other hand, when the chip's thermal power loss is high, the EMVP generated by the heat transfer process dominates. Future research will include investigating ways to decouple these two types of EMVP signals through sensor design, sensor placement, and signal feature extraction, thus improving the monitoring of device health status.

References

[1] F. Blaabjerg, Y. Yang, K. A. Kim, and J. Rodriguez, "Power electronics technology for large-scale renewable energy generation," *Proc. IEEE*, vol. 111, no. 4, pp. 335–355, Apr. 2023.

[2] F. Blaabjerg, Z. Chen, and S. Kjaer, "Power electronics as efficient interface in dispersed power generation systems," *IEEE Trans. Power Electron.*, vol. 19, no. 5, pp. 1184–1194, Sep. 2004.

[3] J. M. Maza-Ortega, E. Acha, S. García, and A. Gómez-Expósito, "Overview of power electronics technology and applications in power generation transmission and distribution," *J. Modern Power Syst. Clean Energy*, vol. 5, no. 4, pp. 499–514, 2017.

[4] Y. Yang, X. Ding, Y. Wu, Z. Shan, G. Lyu, and P. Zhang, "A novel temperature sensitive electrical parameter of IGBT modules without involvement of operating parameters," *IEEE Trans. Electron Devices*, vol. 70, no. 8, pp. 4286–4292, Aug. 2023.

[5] Y. Yang, X. Ding, G. Sun, G. Lyu, and P. Zhang, "IGBT junction temperature monitoring method current calibration free based on the narrow pulse injection," *IEEE Trans. Ind. Electron.*, vol. 71, no. 9, pp. 11475–11487, Sep. 2024.

[6] E. Chiodo and D. Lauria, "Some basic properties of the failure rate of redundant reliability systems in industrial electronics applications," *IEEE Trans. Ind. Electron.*, vol. 62, no. 8, pp. 5055–5062, Aug. 2015.

[7] Y. Song and B. Wang, "Survey on reliability of power electronic systems," *IEEE Trans. Power Electron.*, vol. 28, no. 1, pp. 591–604, Jan. 2013.

[8] S. Yang, D. Xiang, A. Bryant, P. Mawby, L. Ran, and P. Tavner, "Condition monitoring for device reliability in power electronic converters: A review," *IEEE Trans. Power Electron.*, vol. 25, no. 11, pp. 2734–2752, Nov. 2010.

[9] S. Mollov and F. Blaabjerg, "Condition and health monitoring in power electronics," in *Proc. CIPS; 10th Int. Conf. Integr. Power Electron. Syst.*, VDE, 2018, pp. 1–8.

[10] B. Ji, V. Pickert, W. Cao, and B. Zahawi, "In situ diagnostics and prognostics of wire bonding faults in IGBT modules for electric vehicle drives," *IEEE Trans. Power Electron.*, vol. 28, no. 12, pp. 5568–5577, Dec. 2013.

[11] B. Yu and L. Wang, "Online accurate measurement of steady-thermal resistance of SiC mosfets for DC solid-state power controller," *IEEE Trans. Power Electron.*, vol. 36, no. 5, pp. 5006–5021, May 2021.

[12] U.-M. Choi, F. Blaabjerg, F. Iannuzzo, and S. Jørgensen, "Junction temperature estimation method for a 600V, 30A IGBT module during converter operation," *Microelectronics Rel.*, vol. 55, no. 9–10, pp. 2022–2026, 2015.

[13] H. Yang, Y. Chen, Y. Shang, C. Yu, and Y. Kang, "A temperature monitoring method for power electronic converter based on infrared image and object detection algorithm," *IEEE Trans. Ind. Appl.*, vol. 59, no. 1, pp. 1090–1099, Jan./Feb. 2023.

[14] T. E. Salem, D. Ibitayo, and B. R. Geil, "Validation of infrared camera thermal measurements on high-voltage power electronic components," *IEEE Trans. Instrum. Meas.*, vol. 56, no. 5, pp. 1973–1978, Oct. 2007.

[15] N. N. Mai-Khanh, S. Nakajima, T. Iizuka, Y. Mita, and K. Asada, "Noninvasive localization of IGBT faults by high-sensitivity magnetic probe with RF stimulation," *IEEE Trans. Instrum. Meas.*, vol. 67, no. 4, pp. 745–753, Apr. 2018.

[16] F. Benyoubi, L. Pichon, M. Bensetti, Y. Le Bihan, and M. Feliachi, "An efficient method for modeling the magnetic field emissions of power electronic equipment from magnetic near field measurements," *IEEE Trans. Electromagn. Compat.*, vol. 59, no. 2, pp. 609–617, Apr. 2017.

[17] T. J. Kärkkäinen et al., "Acoustic emission in power semiconductor modules—First observations," *IEEE Trans. Power Electron.*, vol. 29, no. 11, pp. 6081–6086, Nov. 2014.

[18] T. J. Kärkkäinen, J. P. Talvitie, O. Ikonen, M. Kuisma, P. Silventoinen, and E. Mengotti, "Sounds from semiconductors - acoustic emission experiment with a power module," in *Proc. 16th Eur. Conf. Power Electron. Appl.*, 2014, pp. 1–6.

[19] M. Kozak and R. Gordon, "Experimental investigations of monolithic IGBT transistor acoustic emission phenomena," *ITM Web Conf.*, vol. 28, 2019, Art. no. 01036, doi: 10.1051/itmconf/20192801036.

[20] A. Bejger, M. Kozak, and R. Gordon, "Acoustic emission of monolithic IGBT transistors," *New Trends Prod. Eng.*, vol. 1, no. 1, pp. 755–760, 2018, doi: 10.2478/ntpe-2018-0095.

[21] R. Gordon and A. Bejger, "Effect of temperature change on acoustic emission signal in IGBT transistors of marine propulsion system converters," *Energies*, vol. 15, no. 12, 2022, Art. no. 4276.

[22] M. Li et al., "Acoustic emission-based experimental analysis of mechanical stress wave in IGBT device," *IEEE Sensors J.*, vol. 20, no. 11, pp. 6064–6074, Jun. 2020.

[23] Y. Bai et al., "Analysis of the stress-wave influence parameters of silicon MOSFET under 300V drain source voltage," *IEEE Sensors J.*, vol. 21, no. 18, pp. 20107–20118, Sep. 2021.

[24] X. Geng et al., "Analysis of influence parameters of stress wave at the turn-off moment in IGBT device based on differential AE sensor," *IEEE Sensors J.*, vol. 22, no. 3, pp. 2259–2270, Feb. 2022.

[25] S. Müller, C. Drechsler, U. Heinkel, and C. Herold, "Acoustic emission for state-of-health determination in power modules," in *Proc. 13th Int. Multi-Conf. Syst., Signals Devices*, IEEE, 2016, pp. 468–471.

[26] P. Davari, O. Kristensen, and F. Iannuzzo, "Investigation of acoustic emission as a non-invasive method for detection of power semiconductor aging," *Microelectronics Rel.*, vol. 88, pp. 545–549, 2018.

[27] A. Bejger, M. Kozak, and R. Gordon, "The use of acoustic emission elastic waves as diagnosis method for insulated-gate bipolar transistor," *J. Mar. Eng. Technol.*, vol. 19, no. 4, pp. 186–196, 2020.

[28] M. Kozak and R. Gordon, "A novel method for diagnosing power electronics devices using elastic wave emission," *Energies*, vol. 16, no. 21, 2023, Art. no. 7405.

[29] X. Geng et al., "Theoretical study on the generation of switching stress waves in power semiconductor devices," *IEEE Trans. Power Electron.*, vol. 38, no. 3, pp. 3939–3950, Mar. 2023.

[30] P. C. Chou and N. J. Pagano, *Elasticity: Tensor, Dyadic, and Engineering Approaches*. San Francisco, CA, USA: Courier Corporation, 1992.

Shuzhi Wen (Student Member, IEEE) received the B.E. degree from School of Automation Science and Electrical Engineering, Beihang University, Beijing, China, in 2021. He is currently working toward the Ph.D. degree in electrical engineering with the Department of Electrical Engineering, Tsinghua University, Beijing.

His research interests include nondestructive testing of power equipment and equipment performance safety assessment.

Bingkun Wei (Member, IEEE) received the Ph.D. degree in materialogy from the College of Materials Science and Opto-Electronic Technology, University of Chinese Academy of Sciences, Beijing, China, in 2024.

He is currently a Research Associate with the Department of Electrical Engineering, Tsinghua University. His major research interests are MEMS sensors and electromagnetic measurement and nondestructive evaluation.

Lisha Peng (Senior Member, IEEE) received the Ph.D. degree in electrical engineering from the Department of Electrical Engineering, Tsinghua University, Beijing, China, in 2019.

She is currently an Assistant Researcher with the Department of Electrical Engineering, Tsinghua University. She is the Deputy Director of Advanced Electrical Technologies Institute, the Deputy Secretary General of the Electromagnetic Testing Technology and Equipment Professional Committee in CES, and the Member of the Chinese society for nondestructive testing. She was selected for the Young Elite Scientists Sponsorship Program by CAST. Her research interests include electromagnetic nondestructive testing and evaluation, intelligent sensor, and signal processing technology.

Pu Huang received the Ph.D. degree in measuring and testing technologies and instruments from the School of Instrumentation and Optoelectronic Engineering, Beihang University, Beijing, China, in 2024.

He is currently a Research Associate with the Department of Electrical Engineering, Tsinghua University. His research interests include electromagnetic nondestructive testing and evaluation, electromagnetic tomography, and deep learning.

Shisong Li (Senior Member, IEEE) received the Ph.D. degree in electrical engineering from Tsinghua University, Beijing, China, in 2014.

Since 2008, he has been involved in a worldwide research project, now known as the Kibble balance experiment, when he was a Researcher with the National Institute of Metrology (NIM), Beijing. During 2014 to 2016, he was a Postdoctoral Researcher with Tsinghua University. He was also a Guest Scholar during September 2013–March 2014, March–September 2015, and April–May 2016, respectively, with the National Institute of Standards and Technology (NIST), Gaithersburg, MD, USA. In September 2016, he joined the Bureau International des Poids et Mesures (BIPM), Svres, France, as a Physicist in mass and electricity metrology. He is currently an Assistant Professor with the Department of Electrical Engineering, Tsinghua University.

Songling Huang (Senior Member, IEEE) received the Ph.D. degree in nuclear application technology from Tsinghua University, Beijing, China, in 2001.

He is currently a Professor with the Department of Electrical Engineering, Tsinghua University. He is also the Director of the Institute of New Electrical Technology and the Leader of the electromagnetic testing and equipment performance safety assessment team. His research interests include high-resolution detection of oil and gas pipeline corrosion defects, stress concentration detection and evaluation, active defect detection, pulsed Eddy current detection sensor, and pipeline defect quantification and safety assessment.